

The keys unlocking redispersion of reactive PdO_x nanoclusters on Ce-functionalized perovskite oxides for methane activation

Yanling Yang^{a, b, #}, Li Zhang^{a, b, #}, Hongquan Guo^b, Zhenfa Ding^b, Weitao Wang^c, Jianhui Li^d, Liujiang Zhou^c, Xin Tu^{c, *}, Yongfu Qiu^{a, *}, Gui Chen^a and Yifei Sun^{b, f, g, *}

^a School of Environment and Civil Engineering, Dongguan University of Technology, Dongguan 523808, China

^b College of Energy, Xiamen University, Xiamen 361005, China

^c Department of Electrical Engineering and Electronics, University of Liverpool, Liverpool L69 3GJ, UK

^d Department of Chemistry, College of Chemistry and Chemical Engineering, Xiamen University, Xiamen 361005, China

^e Institute of Fundamental and Frontier Sciences, University of Electronic Science and Technology of China, Chengdu 610054, China

^f State Key laboratory of physical Chemistry of Solid Surface, Xiamen University, Xiamen 361005, China

^g Shenzhen Research Institute of Xiamen University, Shenzhen 518057, China

Corresponding authors' email: xin.tu@liverpool.ac.uk; qiuyf@dgut.edu.cn; yfsun@xmu.edu.cn

[#] Y.Y. and L.Z. contributed equally to this work.

ABSTRACT

Nowadays, trace CH₄ emitted from vehicle exhausts severely threaten the balance of the ecology system of our earth. Thereby, the development of active and stable catalysts capable of methane conversion under mild conditions is critical. Here, we present a convenient method to redisperse catalytically inert PdO nanoparticles (NPs) (>10 nm) into reactive PdO_x nanoclusters (~2 nm) anchored on Ce doped LaFeO₃ parent.

Isothermally activated in an N₂ flow, the redispersed catalyst achieved a CH₄ conversion of 90% at 400 °C which is significantly higher than the fresh, H₂- and O₂-treated counterparts (625, 616 and 641 °C, respectively), indicating the importance of gas atmosphere in the redispersion of PdO NPs. In addition, the comprehensive catalyst characterizations demonstrated that the isolated Ce ions in the perovskite lattice play an irreplaceable role in the redispersion of reactive sites and the reduction of the energy barrier for C-H scission. More importantly, Ce additive helps to stabilize the PdO_x species by reducing overoxidation, resulting in a significant lifetime extension. Through a thorough understanding of structural manipulation, this work sheds light on the design of highly performing supported catalysts for methane oxidation.

KEYWORD: *CH₄ oxidation, perovskite oxides, Ce doping, redispersion, PdO_x nanoclusters*

1. INTRODUCTION

With the increase of global shale gas production, methane, the main constituent of cheap natural gas, has seen a boom in industrial applications and economic market, such as steam reforming of methane for hydrogen production and methane activation to olefins and aromatics.¹⁻³ Meanwhile, methane is increasingly used as a fuel in industrial heating and vehicle engines. However, the release of trace amounts of unburned methane has a significant greenhouse effect, nearly 22 times that of carbon dioxide.⁴⁻⁵ As a result, it is of significance to use direct flame combustion at low temperatures not only to effectively eliminate the greenhouse gas, but also to avoid the generation of toxic pollutants emitted at high temperatures, such as NO_x and CO.

Because of their lower energy barrier for simultaneous activation of inert C-H

bonds and molecule oxygen, supported Pd catalysts are currently considered as the most promising candidate for converting methane at low temperatures.⁶⁻⁹ Recent studies have highlighted that the metastable Pd-PdO (PdO_x) hybrid phase is the real reactive sites for CH₄ conversion, and the intrinsic catalytic activity of Pd sites has a volcanic shape that is size dependent.¹⁰⁻¹² In addition, it was reported that electron transfer from metal to support was significantly facilitated when the metal particle contained only a few atoms.¹³ Therefore, Pd nanoclusters that are strongly bonded to the support are more favorable for methane activation. At present, supported Pd-based catalysts are primarily synthesized through impregnation and co-precipitation, which are difficult to control the morphology of Pd particles.¹⁴⁻¹⁵ In addition, due to the low adhesion energy to support, Pd nanoclusters are susceptible to sintering.¹⁶ Therefore, it is of great significance to investigate novel strategy for constructing stable supported Pd catalysts with high intrinsic activity.

The redispersion of active metals *via* alternant oxidation/reduction treatment is a promising approach for reconstructing catalytically active sites.¹⁷⁻¹⁸ Specifically, oxidation causes ion diffusion and the formation of metal oxide, followed by reduction (usually in a short time) to form metallic phase. Because sintering is more severe in a reducing environment, the redispersion treatment usually needs to be completed quickly. In addition to treatment conditions, the strong interaction between the support and the metal is required to stabilize the redispersed particles *via* the anchoring effect. For instance, Tanabe et al.¹⁹ reported that the formation of Mg₂PtO₄-like compounds was the driving force for the redispersion of Pt on the MgO surface. Wu et al.²⁰ discovered that Pt redispersion occurred only on ceria cubes with an exposed (100) facet. In contrast, the octahedra ceria with exposed (111) facet exhibited little redispersion phenomena in either an oxidation or a reduction atmosphere. Further research

demonstrated that the (100) facet of ceria could provide a thermodynamically favorable geometry for stabilizing Pt^{2+} by bonding to O^{2-} in square pockets with atomic dispersion and exceptionally high stability.²¹ More impressively, Pt nanoparticles (NPs) on Al_2O_3 support can be redispersed onto adjacent CeO_2 support *via* oxidative calcination because the vacancies on CeO_2 is capable to trap the Pt atoms.²² These findings indicate that the strong interaction between the carrier and the metal helps to determine the redispersion and stability of dispersed metal. Until now, the redispersion of Pd active sites has been achieved through either oxidation/reduction, or chlorination/oxychlorination.²³⁻²⁵ However, due to high energy consumption, poor controllability, and residues of harmful Cl ions, practical application of these methods remains challenging. Exploration of a convenient and effective redispersion route is therefore important.

Perovskite-type oxides, in the formula of ABO_3 with dodecahedral and octahedral coordination for A and B sites, respectively, have been considered as one kind of promising catalyst support, due to their flexible oxygen stoichiometry over a wide range of working temperatures. Lanthanum ferrite (LaFeO_3), for example, has received a lot of attention due to its stable structure and high concentration of oxygen vacancies.²⁶⁻²⁷ More importantly, the La cation and Fe cation can be substituted by other aliovalent cations (e.g., Sr or Ce for the A site and Co, Cu, Ni, Pd or Pt for the B site) to further manipulate the surface defects and electronic configuration of the material.²⁸⁻²⁹ Nishihata et al.³⁰ has reported that the cycling treatment of $\text{LaFe}_{0.57}\text{Co}_{0.38}\text{Pd}_{0.05}\text{O}_3$ catalyst in consecutive oxidative and reductive atmospheres can enable the reversible movement of palladium ions into and out of the perovskite lattice, and O vacancies play a key role in the migration of Pd atoms. Further study revealed that O vacancies stabilized the isolated precious-metal cluster on the surface.³¹ Doping Ce in the A site

of LaFeO_3 perovskite oxide can effectively increase the concentration of oxygen vacancies,³²⁻³³ which may benefit the redispersion process on perovskite systems.

Herein, we prepared Ce doped $\text{LaFe}_{0.97}\text{O}_3$ perovskite oxides and used them as a carrier to achieve the redispersion of Pd species to nanoclusters (Figure 1a). We investigated the catalytic activity and thermal stability of Pd nanoclusters formed under different oxygen partial pressures. Our findings indicate that PdO NPs can be redispersed on Ce doped perovskite oxides, most likely due to the strong interaction between Pd and Ce, which benefits from the highly dispersed Ce species derived from the doping in A site of $\text{LaFe}_{0.97}\text{O}_3$. Low oxygen partial pressure atmosphere can be considered as the driving force for the redispersion of PdO NPs (~10 nm) into nanoclusters. Ce species contributes to maintaining the appropriate chemical state of Pd, which not only stabilizes Pd nanoclusters in certain sizes but also improve their activity.

2. EXPERIMENTAL SECTION

2.1. Catalyst preparation. The $\text{La}_{0.9}\text{Ce}_{0.1}\text{Fe}_{0.97}\text{O}_3$ and $\text{LaFe}_{0.97}\text{O}_3$ perovskite samples were prepared using a sol-gel method. To prepare an aqueous metal salt solution ($0.05 \text{ mol}\cdot\text{L}^{-1}$), a stoichiometric amount of metal nitrate precursors of $\text{La}(\text{NO}_3)_3\cdot 6\text{H}_2\text{O}$ (Macklin, >99%), $\text{Ce}(\text{NO}_3)_3\cdot 6\text{H}_2\text{O}$ (Energy Chemical, 99%) and $\text{Fe}(\text{NO}_3)_3\cdot 9\text{H}_2\text{O}$ (Energy Chemical, 99%) with a molar ratio of 90:10:97 (100:0:97 for $\text{LaFe}_{0.97}\text{O}_3$) were completely dissolved into a certain amount of deionized water. The citric acid was then added to the above solution and completely dissolved (molar ratio of total metal ions/citric acid is 1:2). The obtained solution was stirred at 80 °C until a honey-comb-like gel formed. The gel was then completely dried in an oven at 100 °C overnight. The obtained material was finely ground and calcined in air for 4 h at 800 °C

at a ramping rate of $5\text{ }^{\circ}\text{C}\cdot\text{min}^{-1}$. After natural cooling, the as-prepared brown powders were denoted as LCFO_3 and LFO_3 . The Pd/LCFO_3 and Pd/LFO_3 catalysts were prepared by impregnating $0.37\text{ mg } (\text{NH}_4)_4\text{Pd}(\text{NO}_3)_6$ (Energy Chemical, 99%) on LCFO_3 and LFO_3 (1 g each), respectively, and calcinated at $800\text{ }^{\circ}\text{C}$ for 2 h at a ramping rate of $5\text{ }^{\circ}\text{C}\cdot\text{min}^{-1}$. The other perovskite supported Pd catalysts were all prepared in the same way.

Upon redispersion procedure, the catalyst powder was placed in a ceramic crucible and heated from room temperature to $200\text{ }^{\circ}\text{C}$ at a ramping rate of $5\text{ }^{\circ}\text{C}\cdot\text{min}^{-1}$ using different gas atmospheres such as 5 vol.% H_2/N_2 , pure N_2 , 5 vol. % O_2/N_2 (the total gas flow rate $50\text{ mL}\cdot\text{min}^{-1}$). The as-prepared samples were labeled as $\text{Pd/LFO}_3\text{-H}_2$, $\text{Pd/LFO}_3\text{-N}_2$ and $\text{Pd/LFO}_3\text{-O}_2$, respectively. After 60 min of pre-treatment, the catalyst was heated to $850\text{ }^{\circ}\text{C}$ by staying at $50\text{ }^{\circ}\text{C}$ intervals for 60 minutes.

2.2. Catalytic activity testing. The activities of all the catalysts in methane combustion (light-off test) were measured using a conventional fixed-bed flow reactor (inside diameter: 5 mm) operating at atmospheric pressure. A K-type thermocouple was placed in the middle region of the reactor to monitor the reaction temperature. 100 mg of fresh catalysts (40-60 mesh sizes) were placed in the center of the quartz tube and each side was plugged with quartz cotton. The quartz tube was placed in a tube furnace that was temperature-controlled by an automatic thermometer (Yudian AI708PFKSL2). The gas products were analyzed by gas chromatography (GC, Ruimin 2060 GC) equipped with a hydrogen flame ionization detector (FID). Prior to the measurements, each as-prepared sample was pretreated in 5 vol.% O_2/N_2 at $200\text{ }^{\circ}\text{C}$ for 2 h. The sample was then swept for 0.5 h with pure N_2 . The reaction gas was introduced at a total flow

rate of 50 mL·min⁻¹ (gas hourly space velocity (GHSV) of 30000 mL·g_{cat}⁻¹·h⁻¹) with 1.2 vol% CH₄, 6 vol% O₂ (stoichiometric conditions), and balanced N₂. The catalyst was stabilized for 15 min at each measured temperature point before analyzing the activity.

The conversion of CH₄ was calculated according using the following equation (eq.1):

$$CH_4 \text{ conversion (\%)} = (CH_{4,in} - CH_{4,out}) / CH_{4,in} \times 100 \quad (\text{eq.1})$$

To ensure a kinetically controlled regime and eliminate thermal and diffusion effects, the reaction kinetics were studied with a CH₄ conversion of less than 10%. The reaction rates (r) were calculated using the equation (eq.2):

$$r_{CH_4} = (C_{CH_4} \times X_{CH_4} \times Q \times M_{Pd}) / V_m \times m_{cat} \times w_{Pd} \quad (\text{eq.2})$$

where m_{cat} is the mass of the catalyst used for measurement, w_{Pd} is the Pd loading amount calculated by initial feeding content, C_{CH_4} is the concentration of CH₄ in the feed gas, Q represents total flow rate, V_m is the molar volume of gas, X_{CH_4} is the conversion of CH₄, and M_{Pd} is the atomic weight of Pd (106.4 g·mol⁻¹).

The activation energy (E_a) was calculated by plotting lines to the Arrhenius equation for temperature-dependent vs CH₄ conversion rate (r). To ensure the reliability of the data, the determination coefficient (R^2) for these Arrhenius plots is at least 0.99.

2.3. Material characterization. Powder X-ray diffraction (XRD) patterns of the catalysts were obtained using a Panalytical X'pert PRO diffractometer (Philips, Netherlands) with a Cu K α radiation ($\lambda = 0.15406$ nm) at a voltage of 40 kV and a current of 30 mA.

To investigate the interaction between Pd and perovskite supports, H₂ temperature-programmed reduction (H₂-TPR) experiments were carried out in a homemade fixed-

bed reactor. 100 mg of the catalyst was pretreated in N_2 ($30 \text{ mL}\cdot\text{min}^{-1}$) at 300°C for 1 h. After cooling to room temperature, a 5 vol.% H_2/Ar flow ($20 \text{ mL}\cdot\text{min}^{-1}$) was introduced and kept for about 2 h until the TCD signal became smooth. The H_2 -TPR experiment was then conducted by heating the sample from 30 to 800°C at a heating rate of $5^\circ\text{C}\cdot\text{min}^{-1}$.

The nitrogen isothermal adsorption and desorption experiments were performed on an automated Micromeritics ASAP2020 Plus instrument (Norcross, USA) at -196°C .

Temperature-programmed decomposition (TPD) experiments in N_2 were carried out on a homemade fixed-bed reactor that was connected to an OmnistarTM on-line mass spectrometer (MS, Pfeiffer vacuum, USA) instrument to monitor the O_2 signal ($m/z=32$) in the redispersion treated process. 200 mg of the sample was heated from 30 to 800°C (ramping rate of $5^\circ\text{C}\cdot\text{min}^{-1}$) in flowing N_2 (flow rate of $20 \text{ mL}\cdot\text{min}^{-1}$) and kept at 800°C for 1 hour.

Diffuse reflectance infrared Fourier transform (DRIFT) spectroscopy was performed on a Nicolet iS50 (ThermoFisher, USA) spectrometer equipped with an HVC-MRA-5 reaction chamber (Harrick) and MCT detector. Each sample was reduced at 300°C for an hour in a 5 vol.% H_2/N_2 flow ($50 \text{ mL}\cdot\text{min}^{-1}$) before being purged with N_2 at a flow rate of $50 \text{ mL}\cdot\text{min}^{-1}$ until it reached room temperature. The reaction chamber was then filled with 5 vol.% CO/N_2 ($20 \text{ mL}\cdot\text{min}^{-1}$) and the IR signal was collected using the background spectrum taken in the N_2 atmosphere. After 30 min, the CO flow was replaced by N_2 and maintained for another 20 min until the signal of gas-phase CO disappeared.

The X-ray photoelectron spectroscopy (XPS) characterization was performed on

the ESCALABTM XI⁺ instrument (ThermoFisher, USA) using an Al K α irradiation source at 5.0×10^{-9} mbar. All binding energy values were standardized using the C 1s signal at 284.8 eV.

X-ray absorption near-edge structure (XANES) characterization for the O K edge and the Fe L edge was collected using the Beamlines MCD-A and MCD-B (Soochow Beamline for Energy Materials) at National Synchrotron Radiation Laboratory (NSRL, China).

To evaluate the morphology of the catalysts, transmission electron microscope (TEM) analysis was conducted on a Tecnai F30 transmission electron microscope (TEM; FEI, U.S.), as well as high-angle annular dark-field scanning transmission electron microscopy (HAADF-STEM) and energy dispersive X-ray (EDX) mapping images.

O₂ temperature-programmed desorption (O₂-TPD) was performed on a Hiden Analytical QIC-20 instrument equipped with a mass spectrometer. Before TPD measurement, each sample (0.1 g) was purged in He (30 mL min⁻¹) at 300 °C for 1 h and cooled to 30 °C, followed by O₂ adsorption (10 vol.% O₂ in He, 50 mL min⁻¹) at room temperature for 1 h. Following that, He gas was introduced (30 mL min⁻¹) until the O₂ signal (m/z=32) baseline was stable. Finally, the O₂-TPD measurement was performed from 30 to 800 °C at a heating rate of 10 °C min⁻¹.

3 RESULTS AND DISCUSSION

3.1 Physicochemical Property. The crystallinities Ce doped LFO₃ perovskite (LCFO₃) catalysts were preliminarily analyzed using XRD. Both LFO₃ and LCFO₃ samples show clear diffraction peaks at 22.7°, 32.3°, 39.8°, 46.3°, 52.0°, 57.5°, 67.5° and 76.7°, corresponding to the (101), (121), (220), (202), (141), (240), (242) and (204)

orthorhombic planes of the LaFeO_3 perovskite standard (PDF#37-1943), without the related diffraction peaks which are assigned to the Pd (PDF#46-1403) and PdO (PDF#41-1107) species, suggesting the formation of LaFeO_3 pure phase (Figure 1b).

When 10 mol% Ce is substituted into the A-site of perovskite, the main peak of (121) plane shifts from 32.22° to 32.26° , as shown in magnifying region profiles from 31.5° to 33.0° . The blue shift of diffraction peak is most likely due to the difference in ionic radius difference between La^{3+} (106.1 pm) and Ce^{4+} (92.0 pm). To investigate the effect of Ce specifically, we performed Rietveld refinement of XRD plots for LFO_3 and LCFO_3 samples (Figure S1), and the lattice parameters of LFO_3 and LCFO_3 samples are shown in Table S1. After Ce doping, the decrease in a, b, and c values from 5.560 Å, 7.863 Å and 5.560 Å to 5.554 Å, 7.855 Å and 7.554 Å, proves that the smaller ionic radius of Ce^{4+} results in a contraction in the lattice constant of LFO_3 . Then, using the crystallographic formula for orthorhombic crystal system, the lattice distance (d) values of (121) plane of LFO_3 and LCFO_3 can be calculated, which are 2.780 Å and 2.777 Å, respectively, as shown in Table S2. According to the Bragg equation, the obtained 2θ values of diffraction peak of (121) plane are 32.18° and 32.22° , which are close to the experimental results with a 0.04° blue shift of the diffraction peak. Therefore, it is confirmed that Ce ions act as a dopant at the La site in the lattice, resulting in a solid solution rather than an isolated CeO_2 bulk phase. The impregnation of Pd species on the LFO_3 and LCFO_3 samples had no effect on the crystallinity of perovskite, signifying that Pd species can exist on perovskite oxides without being doped into the lattice. Moreover, after being treated with N_2 , the XPD patterns of Pd/ LFO_3 and Pd/ LCFO_3 remain unchanged, indicating that the catalysts are robust. However, the weakened hysteresis loop in the N_2 adsorption and desorption curves after Ce doping indicates a change in the microstructure of perovskite (Figure S2). The decreased BET surface area,

pore size and pore volume of the catalysts (Table S1) are attributed to the partially blocked pores by the Pd species with large particle size. All these microstructure parameters increased again when treated with N_2 , which is presumably related to the enhanced density of surface NPs. Figures 1c and 1d show the TEM and HAADF-STEM images of the $LCFO_3$ support with a visible porous structure. The lattice distance of 0.39 nm (Figure 1d) corresponds to the (101) plane of $LaFeO_3$ (PDF#37-1943), evidencing the maintenance of perovskite after Ce doping. Furthermore, the elemental mapping images (Figure 1d) shows that La, Ce, Fe and O are evenly distributed in the skeleton, indicating the formation of a homogeneous solid solution with no visible Ce segregation.

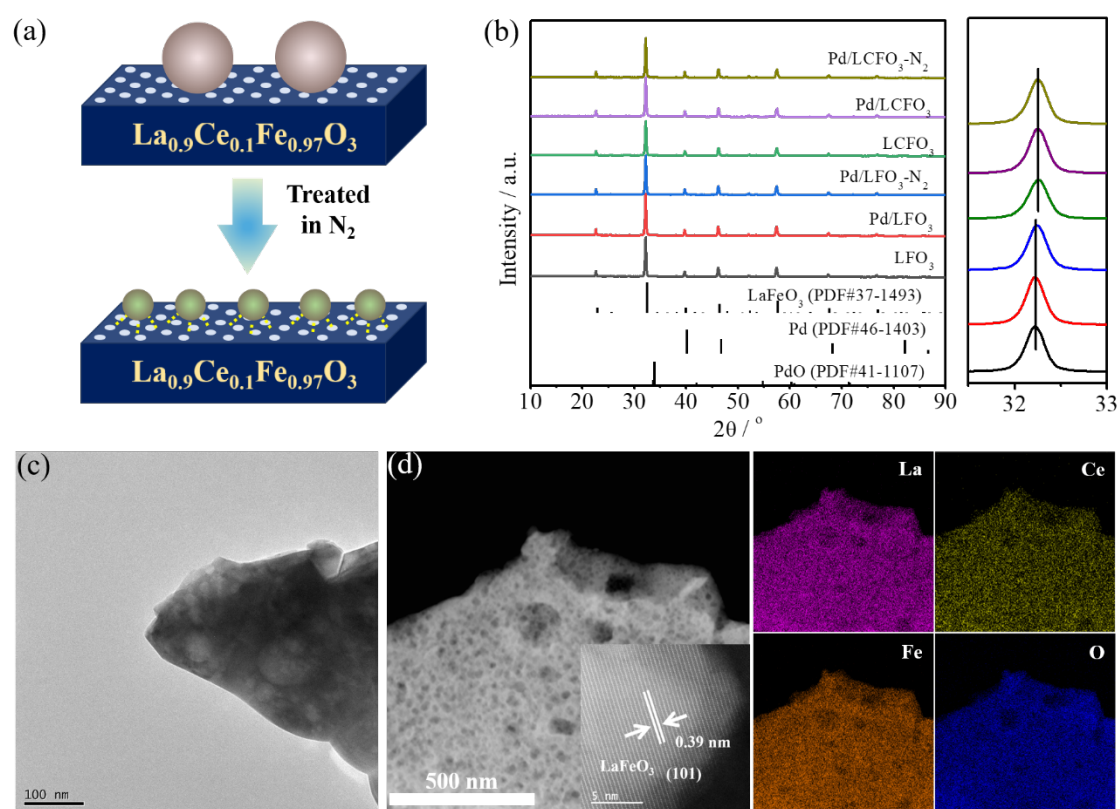


Figure 1. (a) Schematic diagram of the redispersion of Pd species on the $LCFO_3$ surface. (b) The XRD patterns of LFO_3 based Pd catalysts, (c-d) The TEM and HAADF-STEM images of $LCFO_3$ samples with the elemental mapping of La, Ce, Fe and O.

3.2. Redispersal of Pd species on perovskite. Traditional works on the redispersal of supported metal NPs rely heavily on commutative oxidative/reductive atmospheres. Instead, we designed an alternative method to redisperse larger PdO into a small nanocluster in the presence of mild N₂. The Pd species after impregnation and initial calcination are in the form of PdO rather than metallic state.³⁴ XPS was used to analyze the chemical state of Pd species in Ce incorporated catalyst after N₂ treatment. Pd 3d_{3/2} binding energy peak at ~336.7 eV is observed in both Pd/LFO₃ and Pd/LCFO₃, corresponding to the Pd²⁺ species in PdO on the surface of perovskite (Figure 2a). Pd⁰ species (335.1 eV) are clearly present in the Pd/LFO₃-N₂ and Pd/LCFO₃-N₂ catalysts after N₂ treatment,³⁵ suggesting that the oxide is nearly completely transformed to metal. Due to the phase change from oxide to metal, the redispersal process may result in a change in oxygen stoichiometry which must be monitored. As a result, the evolution of O₂ signals during the redispersal process was monitored using online mass spectroscopy (MS), and the results are shown in Figure 2b. Both Pd/LFO₃ and Pd/LCFO₃ samples (300 °C) show weak O₂ consumption signals, which can be attributed to the presence of oxygen vacancies. The remarkable O₂ release signal appears when the temperature is raised to 800 °C for Pd/LFO₃ and 750 °C for Pd/LCFO₃, respectively, whereas there is no distinct O₂ release signal in the MS signals for pure perovskites (Figure S3) when treated in the same conditions. According to equation 3, the loss of O species in the form of O₂ is mainly caused by the decomposition of PdO.



CO in situ diffuse reflectance infrared Fourier transform spectroscopy (CO-DRIFTS) was used to investigate the modality in Pd species of the Pd/LFO₃ and Pd/LCFO₃ samples before and after N₂ treatment. As shown in Figure 2c, the dominant vibrational bands at 1843 and 1897 cm⁻¹ on both the Pd/LFO₃ and Pd/LCFO₃ catalysts

are related to CO multiple adsorptions on Pd⁰, whereas the 1960 cm⁻¹ vibrational band on Pd/LFO₃-N₂ and Pd/LCFO₃-N₂ corresponds to the bridge-adsorption at Pd⁰ sites.¹¹⁻¹² More specifically, the vibrational bands at 1843/1897 cm⁻¹ and 1960 cm⁻¹ represent CO adsorption at the terrace and step sites of Pd particles, respectively. Both vibrational bands show a redshift after N₂ treatment, suggesting the formation of smaller Pd species, especially sub-nanometers. Figure 2d shows the H₂-TPR profiles of Pd/LFO₃ and Pd/LCFO₃ before and after N₂ treatment. The apparent H₂ consumption centered at 80 °C and 50 °C for the Pd/LFO₃ and Pd/LCFO₃ samples manifests the reduction of Pd oxide on the surface of the support,³⁶ since these two peaks are absent on the LFO₃ and LCFO₃ samples (Figure S4). The doping of Ce facilitates the redox property of Pd species by shifting the TPR peak position to lower temperatures. In low temperature regions (< 100 °C), the Pd/LFO₃-N₂ and Pd/LCFO₃-N₂ catalysts show a visible negative hydrogen overflow peak rather than the reduction one, as is commonly on the surface of metallic Pd. Therefore, the TPR and FT-IR results support the hypothesis that the N₂ treatment can efficiently induce the formation of metallic Pd clusters.

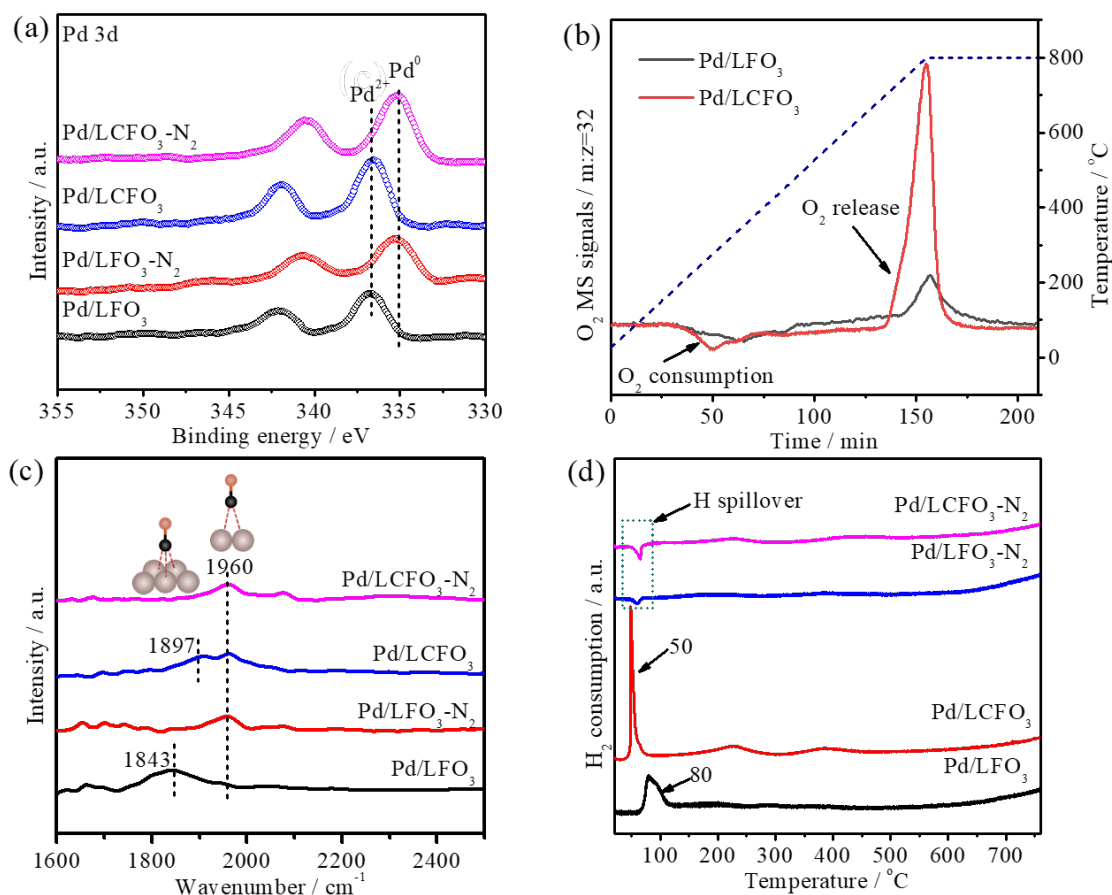


Figure 2. (a) XPS spectra of Pd/LFO₃ and Pd/LCFO₃ before and after N₂ treatment with Pd 3d. (b) MS O₂ signal (mass=32) of Pd/LFO₃ and Pd/LCFO₃ in nitrogen treatment with temperature-programmed process. (c) CO infrared spectra and (d) H₂-TPR profiles of Pd/LFO₃ and Pd/LCFO₃ before and after nitrogen treatment.

Figures 3a, b and 3c, d show the HRTEM and AC-STEM images of the Pd/LCFO₃ sample and Pd/LCFO₃-N₂ treated in reaction gas at 200 °C for 1 h, respectively. Large NPs with a size over 10 nm can be clearly observed on the support (Figure 3a). The exposed lattice distance of 0.26 nm (Figure 3b, red ellipse) and spatial lattice structure derived from the fast Fourier transform (FFT) matched well with the (101) lattice of PdO (PDF#41-1107). Noticeably, Figure 3d shows PdO with an NP size of ~2 nm on the reaction gas treated Pd/LCFO₃-N₂, proving the formation of a smaller size of Pd species after N₂ treatment. Figures 3e and 3f show STEM images of Pd/LCFO₃ and

Pd/LCFO₃-N₂ (treated with reaction gas), as well as elemental mapping images of La, Ce, Fe and Pd. Except for Pd, which has significant segregation, the elements La, Ce and Fe are evenly distributed in the skeleton. A remarkable improvement in the dispersion of Pd species can be found for the homo-dispersed Pd element as well as the La, Ce and Fe (Figure 3f).

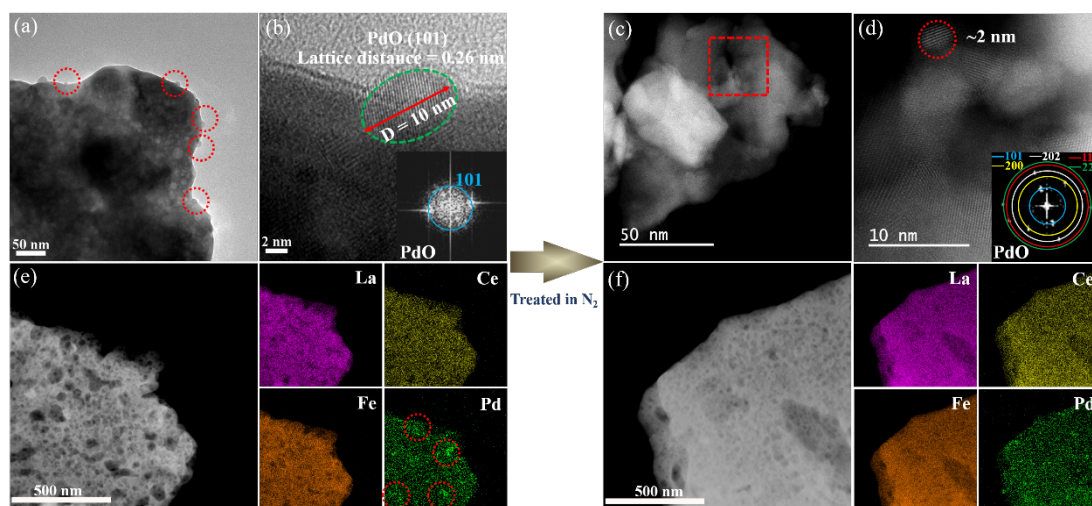


Figure 3. (a, b) The (HR)TEM images of Pd/LCFO₃ and (c, d) Aberration-Corrected Scanning transmission electron microscopy (AC-STEM) images of Pd/LCFO₃-N₂ treated in reaction gas at 200 °C for 1 h. (e, f) HADDF-STEM images and elemental mapping of La, Ce, Fe and O for (e) Pd/LCFO₃ oxide and (f) Pd/LCFO₃-N₂ treated in reaction gas for 1 h.

3.3. Catalytic activity measurement. The catalytic performance of Pd/LFO₃ and Pd/LCFO₃ before and after N₂ treatment was evaluated in methane combustion between 200 and 850 °C (Figure 4a). For further investigation, the optimal redispersion temperature is determined to be 800 °C (Figure S5). Pd/LFO₃ and Pd/LCFO₃ exhibit poor catalytic activity for CH₄ initiation temperatures approaching 450 °C. The CH₄ conversion is remarkably promoted on the redispersed Pd/LFO₃-N₂ catalyst as the initiation temperature is reduced by 150 °C. However, its activity was not stable because

of the decomposition of PdO species at reaction temperature above 450 °C,³⁷ as confirmed by the Pd 3d XPS spectra in Figure S6. Notably, such deactivation can be completely eliminated by Ce incorporation, resulting in enhanced catalytic activity with a lower T_{90} (temperature corresponding to 90% methane conversion) of 443 °C compared to Pd/LFO₃-N₂ (T_{90} , 692 °C). This result demonstrates that the doping of Ce in perovskite plays a critical role in enhancing catalytic performance and maintaining active sites. However, compared to Pd/LCFO₃-N₂, the catalyst with impregnated Ce species (Pd-Ce/LFO₃) has a higher T_{50} (384 °C) and T_{90} (472 °C), as shown in Figure S7. Therefore, these results indicate that highly dispersed Ce species are more effective at catalyzing the conversion of CH₄ than isolated CeO₂ NPs (Figure S8-9).

Kinetic experiments were carried out to investigate the intrinsic differences in the catalytic activity of these catalysts (Pd content was determined by ICP-OES analysis, as shown in Table S3), and the associated activation energy results are presented in Figure 4b. The activation energy of Pd/LFO₃ and Pd/LCFO₃ before and after N₂ treatment is 178.9, 78.1, 135.5 and 52.2 kJ mol⁻¹, respectively. The Pd/LCFO₃-N₂ sample has the lowest value, revealing increased activity of the individual reactive sites, which is consistent with the highest catalytic activity of Pd/LCFO₃-N₂, especially at low temperatures. Furthermore, the Pd/LCFO₃-N₂ catalyst exhibits excellent stability, with a negligible change in CH₄ conversion (28-30%) over a 20 h time-on-stream experiment at 350 °C, which is much stronger than Pd/LFO₃-N₂ (decline by 44.1%) (Figure 4c). The reversibility of the redispersion process is demonstrated by re-calcining the catalyst in an oven and treating it with nitrogen gas again (cycle 2). Figure 4d depicts the T_{90} of Pd/LFO₃-N₂ and Pd/LCFO₃-N₂ after two cycles testing. The T_{90} s of both samples in cycle 2 are nearly identical to those of cycle 1, suggesting the redispersion of PdO is reproducible.

Since Ce doped LFO₃ perovskite can effectively realize the redispersion of Pd species, the carrier effect merits further investigation. Firstly, La₂O₃, CeO₂ and Fe₂O₃ were used as supports for prepared catalysts with equal Pd loading, and those samples were also treated under identical N₂ conditions. Pd/La₂O₃-N₂, Pd/CeO₂-N₂ and Pd/Fe₂O₃-N₂ (taken from Figure S10) have T₉₀ values of 698, 520 and 632 °C, respectively, which do not differ significantly from Pd/La₂O₃, Pd/CeO₂ and Pd/Fe₂O₃ (Figure 4e). In addition, the T₉₀ values listed above are all much higher than those obtained with the Pd/LCFO₃-N₂ catalyst. Other perovskite oxide supports such as Ce (un)doped LaMn_{0.97}O₃ and PrMn_{0.97}O₃ (abbreviated to L(C)MO₃ and P(C)MO₃, respectively) were prepared by the sol-gel method and served as a platform to redisperse Pd species. The T₉₀ of Pd/LMO₃-N₂ and Pd/PMO₃-N₂ decreases significantly when compared to that of samples without N₂ treatment. Similar to the Pd/LCF system, Ce doped PMO₃ and LMO₃ displayed enhanced activity and stability when compared to counterparts without Ce in the lattice (Figure 4e and Figure S11). According to the findings, perovskite oxides are more conducive to facilitating the redispersion of PdO with large scale size, as opposed to traditional oxide carriers, and Ce doping in perovskite can stabilize these PdO_x nanoclusters after dispersion.

3.4. The effect of redispersion atmosphere. We have shown that Pd species can be favorably redispersed on Ce doped perovskite oxides using N₂ treatment; it will be interesting to understand if other atmospheres can serve as a driving force to trigger redispersion. Figure 4f depicts the CH₄ conversions at 400 °C using Pd/LCFO₃ treated in various atmospheres (derived from the CH₄ conversion curves in Figure S12). When Pd/LCFO₃ was treated in 5 vol.%O₂/N₂, the CH₄ conversion at 400 °C (22.6%) is nearly two times higher than that of untreated Pd/LCFO₃ (11.7%), but still far lower than that of N₂ treated samples (80.3%). The XRD and TEM results of the Pd/LCFO₃ sample

treated with 5 vol.% O₂/N₂ confirm that the main crystal structure of perovskite is preserved (Figure S13-14). While the obvious reduction peak (53.5 °C) in low temperature (Figure S15) can be attributed to the reduction of palladium oxide, the overoxidized Pd species may not be efficient centers of catalytic activity like the Pd/LCFO₃ sample. Switching to a weaker oxidizing atmosphere of 3 vol.% H₂O/N₂, the CH₄ conversion at 400 °C reaches 70.0%, similar to the catalyst treated in N₂ (80.3%). Therefore, this finding reveals that the oxidative environment is not beneficial for the formation of active sites, but rather produces excessive palladium oxide instead of a Pd-PdO mixed phase.³⁴ To reduce the oxygen partial pressure, the N₂ was dehydrated with a purifier containing a 5A molecular sieve and deoxygenated with a manganese-based adsorbent. At 400 °C, dehydrated nitrogen (N₂(_{de}H₂O)) and dehydrated-deoxygenated nitrogen (N₂(_{de}H₂O+_{de}O₂)) can improve the CH₄ conversion to 87.3% and 92.4%, respectively. Based on these results, we hypothesized that hydrogen gas with an extremely low partial pressure of oxygen would be an excellent redispersion initiator. However, after 5 vol.%H₂/N₂ treatment, the Pd/LCFO₃ was severely inactivated (Figure 4f), with less than 5% conversion of CH₄ at 400 °C, and the collapse of the perovskite phase (Figure S16-17). Therefore, it can be summarized that the low partial pressure of oxygen in a mild insert gas is critical to achieving the redispersion of Pd species, which not only drives the decomposition of Pd species, but also avoids overoxidized active sites of Pd species in the treated process.

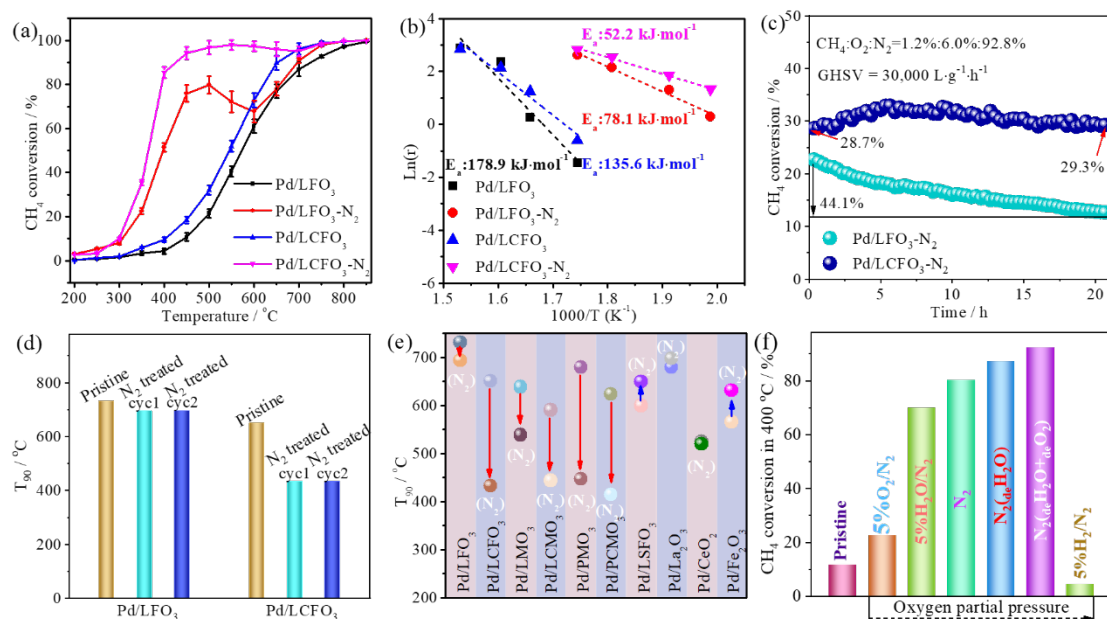


Figure 4. (a) Temperature-dependent CH_4 conversion over Pd/LFO_3 and Pd/LCFO_3 before and after N_2 treatment. (b) Differential reaction rates for CH_4 oxidation with 1.2 KPa CH_4 and 6 KPa O_2 in steady-state for 0.05g samples of N_2 (un)treated Pd/LFO_3 and Pd/LCFO_3 . (c) Catalytic stability of $\text{Pd/LFO}_3\text{-N}_2$ and $\text{Pd/LCFO}_3\text{-N}_2$ performed at 350 °C under GHSV of $30,000 \text{ L}\cdot\text{g}^{-1}\cdot\text{h}^{-1}$. (d) The temperature at 90% conversion of CH_4 (T_{90}) for Pd/LFO_3 and Pd/LCFO_3 after two cycles in N_2 (the T_{90} in cycle 2 was collected after calcination in a muffle oven at 800 °C of cycle 1 tested samples, followed by nitrogen treatment). (e) T_{90} of different types of support Pd supported catalysts before and after nitrogen treatment. (f) The CH_4 conversion of Pd/LCFO_3 treated in 5% H_2/N_2 , 5% O_2 , 5% $\text{H}_2\text{O}/\text{N}_2$, N_2 , dehydrated N_2 ($_{\text{de}}\text{H}_2\text{O}$), and dehydrated and deoxygenated N_2 ($_{\text{de}}\text{H}_2\text{O}+_{\text{de}}\text{O}_2$) at 400 °C.

3.5. The unique role of Ce doping. Aside from the atmosphere, the presence of isolated Ce elements in perovskite influences the redispersion of loaded Pd species and, as a result, the activity of the catalysts. It is well known that oxygen vacancies are effective sites for oxygen activation mechanism in oxidation reactions via the Mar–van

Krevelen (M–vK).³⁸⁻³⁹ Figure 2b shows a certain amount of oxygen vacancies in perovskites for the O₂ consumption at ~300 °C. Therefore, a qualitative comparison of oxygen vacancies before and after Ce doping is required. As shown in Figure 5a, the O 1s spectra of Pd/LFO₃ and Pd/LCFO₃ can be divided into two peaks including lattice oxygen (O_{latt}, 528.7 eV) and active surface-adsorbed oxygen species (O_{ads}, 530.9 eV).⁸

⁴⁰ The O_{latt}/O_{ads} area ratio of Pd/LCFO₃ is 1.33, much higher than that of Pd/LFO₃ (0.80), indicating that Ce doping in the LFO₃ sample can induce more oxygen vacancies. Moreover, the O_{latt}/O_{ads} area ratio of the Pd/LCFO₃-N₂ catalyst is slightly increased after N₂ treatment (increased to 1.54) rather than the Pd/LFO₃-N₂ catalyst (remains at 0.80), indicating more lattice oxygen species in the Pd/LCFO₃-N₂ catalyst. Simultaneously, the valence states of Ce species were examined to estimate the change in oxygen species following N₂ treatment. Figure 5b depicts the Ce 3d XPS spectra, with the peaks marked as u, v series corresponding to Ce 3d_{3/2}, Ce 3d_{5/2}, respectively. The doublet (u', v') is associated with Ce³⁺ species, while the remainders are assigned to Ce⁴⁺.⁴¹⁻⁴² The Ce⁴⁺/Ce³⁺ ratio for Pd/LCFO₃ after N₂ treatment increased from 21.2% to 33.3%, as determined by curves fitting of Ce 3d spectra, indicating an increase in redox-pairs amount, which may be responsible for the high performance in catalytic methane conversion. The XAS was used to investigate the metal-oxygen hybridization status in perovskite, and the normalized O K-edge XANES spectra of Pd/LFO₃ and Pd/LCFO₃ before and after N₂ treatment are shown in Figure 5c. Similar to the literature, the spectra can be divided into three distinct regions. The first ranges from 528 to 533 eV (peak 1) and is described as oxygen 2p states hybridized with transition metal Fe 3d states. The next region, 533–538 eV (peak 2), is explained as the hybridization between oxygen 2p states and La atom 5d states. The region above 538 eV (peak 3) is attributed to orbital overlap between transition metal and La atoms in higher energy states.⁴³⁻⁴⁴

Peaks 1 and 2 are intensified after Ce doping, but barely changed after N₂ treatment, suggesting that metal hybridization with O2p states is strengthened. Soft X-Ray XAS at the Fe-L_{2,3} edge (in Figure 5d) and XPS spectra of Fe 2p (in Figure 5e) were used to confirm the valence state of Fe ion. The coordination status of the contaminant is maintained well (overlapped curve of Fe L-edge), and Fe³⁺ is the main valence state of Fe species with no discernible change in all samples, revealing that the redispersion process in N₂ has no effect on Fe coordination environment and valence state. Given that increased oxygen vacancy content may be the main inducer of enhanced metal-oxygen hybridization following Ce doping, it is necessary to investigate oxygen absorption capability, which is conducive to methane conversion. Figure 5f shows two obvious desorption peaks for Pd/LCFO₃-N₂ at 550 °C and 705 °C, which can be attributed to the weak and strong adsorption of oxygen on the surface of perovskite. The peaks of Pd/LFO₃-N₂ at higher temperatures of 580 °C and 750 °C with adsorption capacity half that of Pd/LCFO₃-N₂ confirm the promoted oxygen capture ability of the Pd/LCFO₃-N₂ catalyst. The above results demonstrate that doping Ce species successfully engineered more vacant oxygen on the Pd/LCFO₃-N₂ surface, which can further alleviate the overoxidation of Pd species after prolonged measurement (Figure S18).

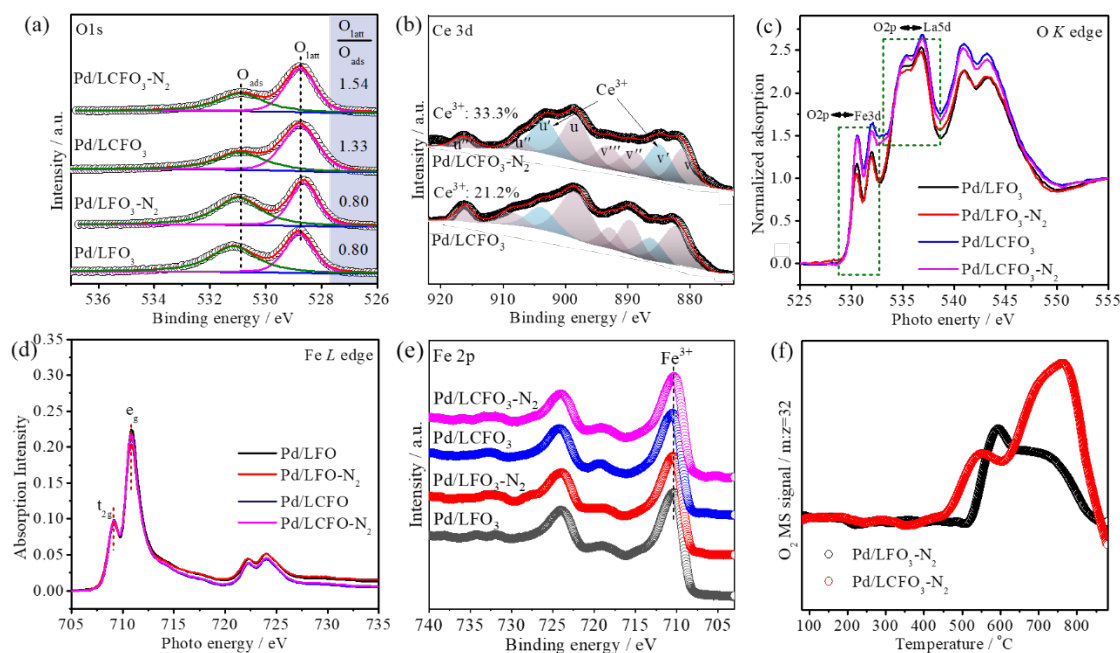


Figure 5. XPS spectra of Pd/LFO₃ and Pd/LCFO₃ before and after N₂ treatment with (a) O 1s and (b) Ce 3d of Pd/LCFO₃ and Pd/LCFO₃-N₂. (c, d) The O K-edge and Fe L-edge XANES spectra of various catalysts. (e) XPS spectra of Fe 2p. (f) The O₂-TPD profiles of Pd/LFO₃-N₂ and Pd/LCFO₃-N₂ catalysts.

4. CONCLUSION

To summarize, we demonstrated a facile method for the redispersion of large PdO NPs (>10 nm) into smaller nanoclusters (<3 nm) with enhanced catalytic activity and durability in methane oxidation. The insert gas is identified as the first key to driving the decomposition of larger Pd species while maintaining the perovskite framework. The Pd/LCFO₃-N₂ catalyst showed a desirable T₉₀ as low as 400 °C, with excellent durability and cyclability. Furthermore, the Ce ions in the perovskite lattice serve as the second key to unlocking the redispersion of Pd species and are beneficial in lowering the energy barrier for the cleavage of C-H bonds. The presence of Ce doping, which acts as an oxygen reservoir, increases the formation of oxygen vacancies, preventing deep oxidation/deactivation of Pd species. This work offers a new avenue for the

rational design and controllable synthesis of high-performance combustion oxide catalysts.

ASSOCIATED CONTENT

Supporting Information

The Supporting Information is available free of charge at xxx.

Additional nitrogen isothermal adsorption and desorption, catalytic activity testing, XRD, temperature-programmed decomposition, H₂-TPR, TEM and XPS characterization results (PDF)

AUTHOR INFORMATION

Corresponding Authors

Xin Tu – *Department of Electrical Engineering and Electronics, University of Liverpool, Liverpool L69 3GJ, UK; Email: xin.tu@liverpool.ac.uk*

Yongfu Qiu – *School of Environment and Civil Engineering, Dongguan University of Technology, Dongguan 523808, China; Email: _qiuyf@dgut.edu.cn*

Yifei Sun – *College of Energy, Xiamen University, Xiamen 361005, PR China; State Key laboratory of physical Chemistry of Solid Surface, Xiamen University, Xiamen 361005, China; Shenzhen Research Institute of Xiamen University, Shenzhen 518057, China; Email: yfsun@xmu.edu.cn*

Authors

Yanling Yang – *School of Environment and Civil Engineering, Dongguan University of Technology, Dongguan 523808, China; College of Energy, Xiamen University, Xiamen 361005, China*

Li Zhang – *School of Environment and Civil Engineering, Dongguan University of*

Technology, Dongguan 523808, China; College of Energy, Xiamen University, Xiamen 361005, China

Hongquan Guo – *College of Energy, Xiamen University, Xiamen 361005, China*

Zhenfa Ding – *College of Energy, Xiamen University, Xiamen 361005, China*

Weitao Wang – *Department of Electrical Engineering and Electronics, University of Liverpool, Liverpool L69 3GJ, UK*

Jianhui Li – *Department of Chemistry, College of Chemistry and Chemical Engineering, Xiamen University, Xiamen 361005, China*

Liuqing Zhou – *Institute of Fundamental and Frontier Sciences, University of Electronic Science and Technology of China, Chengdu 610054, China*

Gui Chen – *School of Environment and Civil Engineering, Dongguan University of Technology, Dongguan 523808, China*

Author Contributions

#Y.Y. and L.Z. contributed equally to this work.

Notes

The authors declare no competing financial interest.

ACKNOWLEDGMENTS

This work was funded by the National Natural Science Foundation of China (No. 22102135) and the Natural Science Foundation of Fujian Province, China (2021J05014). Y. Sun appreciates the Guangdong Basic and Applied Basic Research Foundation (2020A1515110904) for their support. X. Tu gratefully acknowledges the British Council Newton Fund Institutional Links Grant (No. 623389161).

REFERENCES

1. Luo, J. Z.; Yu, Z. L.; Ng, C. F.; Au, C. T., CO₂/CH₄ Reforming over Ni–La₂O₃/5A: An Investigation on Carbon Deposition and Reaction Steps, *J. Catal.* **2000**, *194* (2), 198.
2. Guo, X.; Fang, G.; Li, G.; Ma, H.; Fan, H.; Yu, L.; Ma, C.; Wu, X.; Deng, D.; Wei, M.; Tan, D.; Si, R.; Zhang, S.; Li, J.; Sun, L.; Tang, Z.; Pan, X.; Bao, X., Direct, Nonoxidative Conversion of Methane to Ethylene, Aromatics, and Hydrogen, *Science* **2014**, *344*, 616.
3. Sakbodin, M.; Wu, Y.; Oh, S. C.; Wachsman, E. D.; Liu, D., Hydrogen-Permeable Tubular Membrane Reactor: Promoting Conversion and Product Selectivity for Non-Oxidative Activation of Methane over an Fe(c)SiO₂ Catalyst, *Angew. Chem. Int. Ed.* **2016**, *55* (52), 16149.
4. He, L.; Fan, Y.; Bellettre, J.; Yue, J.; Luo, L., A Review on Catalytic Methane Combustion at Low Temperatures: Catalysts, Mechanisms, Reaction Conditions and Reactor Designs, *Renew. Sustain. Energy Rev.* **2020**, *119*, 109589.
5. Jiang, X.; Mira, D.; Cluff, D. L., The Combustion Mitigation of Methane as a Non-CO₂ Greenhouse Gas, *Prog. Energy Combust. Sci.* **2018**, *66*, 176.
6. Chin, Y. H.; Buda, C.; Neurock, M.; Iglesia, E., Consequences of Metal-Oxide Interconversion for C-H Bond Activation during CH₄ Reactions on Pd Catalysts, *J. Am. Chem. Soc.* **2013**, *135* (41), 15425.
7. Losch, P.; Huang, W.; Vozniuk, O.; Goodman, E. D.; Schmidt, W.; Cargnello, M., Modular Pd/Zeolite Composites Demonstrating the Key Role of Support Hydrophobic/Hydrophilic Character in Methane Catalytic Combustion, *ACS Catal.* **2019**, *9* (6), 4742.
8. Xiong, J.; Yang, J.; Chi, X.; Wu, K.; Song, L.; Li, T.; Zhao, Y.; Huang, H.; Chen, P.; Wu, J.; Chen, L.; Fu, M.; Ye, D., Pd-Promoted Co₂NiO₄ with Lattice Co-O-Ni and

Interfacial Pd-O Activation for Highly Efficient Methane Oxidation, *Appl. Catal. B* **2021**, 292, 120201.

9. Jiang, D.; Khivantsev, K.; Wang, Y., Low-Temperature Methane Oxidation for Efficient Emission Control in Natural Gas Vehicles: Pd and Beyond, *ACS Catal.* **2020**, 10 (23), 14304.

10. Willis, J. J.; Goodman, E. D.; Wu, L.; Riscoe, A. R.; Martins, P.; Tassone, C. J.; Cargnello, M., Systematic Identification of Promoters for Methane Oxidation Catalysts Using Size- and Composition-Controlled Pd-Based Bimetallic Nanocrystals, *J. Am. Chem. Soc.* **2017**, 139 (34), 11989.

11. Murata, K.; Mahara, Y.; Ohyama, J.; Yamamoto, Y.; Arai, S.; Satsuma, A., The Metal-Support Interaction Concerning the Particle Size Effect of Pd/Al₂O₃ on Methane Combustion, *Angew. Chem. Int. Ed.* **2017**, 56 (50), 15993.

12. Chen, J.; Zhong, J.; Wu, Y.; Hu, W.; Qu, P.; Xiao, X.; Zhang, G.; Liu, X.; Jiao, Y.; Zhong, L.; Chen, Y., Particle Size Effects in Stoichiometric Methane Combustion: Structure–Activity Relationship of Pd Catalyst Supported on Gamma-Alumina, *ACS Catal.* **2020**, 10 (18), 10339.

13. Lykhach, Y.; Kozlov, S. M.; Skála, T.; Tovt, A.; Stetsovykh, V.; Tsud, N.; Dvořák, F.; Johánek, V.; Neitzel, A.; Mysliveček, J.; Fabris, S.; Matolín, V.; Neyman, K. M.; Libuda, J., Counting Electrons on Supported Nanoparticles, *Nat. Mater.* **2016**, 15, 284.

14. Zhao, G.; Pan, X.; Zhang, Z.; Liu, Y.; Lu, Y., A Thin-Felt Pd–MgO–Al₂O₃/Al-Fiber Catalyst for Catalytic Combustion of Methane with Resistance to Water-Vapor Poisoning, *J. Catal.* **2020**, 384, 122.

15. Xiao, Y.; Li, J.; Wang, C.; Zhong, F.; Zheng, Y.; Jiang, L., Construction and Evolution of Active Palladium Species on Phase-Regulated Reducible TiO₂ for Methane Combustion, *Catal. Sci. Technol.* **2021**, 11 (3), 836.

16. Su, Y. Q.; Liu, J. X.; Filot, I. A. W.; Hensen, E. J. M., Theoretical Study of Ripening Mechanisms of Pd Clusters on Ceria, *Chem. Mater.* **2017**, 29 (21), 9456.
17. Nagai, Y.; Hirabayashi, T.; Dohmae, K.; Takagi, N.; Minami, T.; Shinjoh, H.; Matsumoto, S., Sintering Inhibition Mechanism of Platinum Supported on Ceria-Based Oxide and Pt-Oxide–Support Interaction, *J. Catal.* **2006**, 242 (1), 103.
18. Morgan, K.; Goguet, A.; Hardacre, C., Metal Redispersion Strategies for Recycling of Supported Metal Catalysts: A Perspective, *ACS Catal.* **2015**, 5 (6), 3430.
19. Toshitaka, T.; Yasutaka, N.; Kazuhiko, D.; Hideo, S.; Hirohumi, S., Sintering and Redispersion Behavior of Pt on Pt/MgO, *J. Catal.* **2008**, 257, 117.
20. Wu, T.; Pan, X.; Zhang, Y.; Miao, Z.; Zhang, B.; Li, J.; Yang, X., Investigation of the Redispersion of Pt Nanoparticles on Polyhedral Ceria Nanoparticles, *J. Phys. Chem. Lett.* **2014**, 5 (14), 2479.
21. Bruix, A.; Lykhach, Y.; Matolinova, I.; Neitzel, A.; Skala, T.; Tsud, N.; Vorokhta, M.; Stetsovych, V.; Sevcikova, K.; Myslivecek, J.; Fiala, R.; Vaclavu, M.; Prince, K. C.; Bruyere, S.; Potin, V.; Illas, F.; Matolin, V.; Libuda, J.; Neyman, K. M., Maximum Noble-Metal Efficiency in Catalytic Materials: Atomically Dispersed Surface Platinum, *Angew. Chem. Int. Ed.* **2014**, 53 (39), 10525.
22. Jones, J.; Xiong, H.; DeLaRiva, A. T.; Peterson, E. J.; Pham, H.; Challa, S. R.; Qi, G.; Oh, S.; Wiebenga, M. H.; Hernández, X. I. P.; Wang, Y.; Datye, A. K., Thermally Stable Single-Atomplatinum-on-Ceria Catalysts via Atom Trapping, *Science* **2016**, 353, 150.
23. Newton, M. A.; Bolver-Coldeira, C.; Martínez-Arias, A.; Fernández-García, M., “Oxidationless” Promotion of Rapid Palladium Redispersion by Oxygen during Redox CO/(NO+O₂) Cycling, *Angew. Chem. Int. Ed.* **2007**, 119 (45), 8783.
24. Kubacka, A.; Iglesias-Juez, A.; Di Michiel, M.; Newton, M. A.; Fernandez-Garcia,

M., Influence of the Ce-Zr Promoter on Pd Behaviour under Dynamic CO/NO Cycling Conditions: A Structural and Chemical Approach, *Phys. Chem. Chem. Phys.* **2013**, *15* (22), 8640.

25. Lambrou, P. S.; Polychronopoulou, K.; Petallidou, K. C.; Efstathiou, A. M., Oxy-Chlorination as an Effective Treatment of Aged Pd/CeO₂-Al₂O₃ Catalysts for Pd Redispersed, *Appl. Catal. B* **2012**, *111-112*, 349.

26. Garcia-Muñoz, P.; Lefevre, C.; Robert, D.; Keller, N., Ti-Substituted LaFeO₃ Perovskite as Photoassisted CWPO Catalyst for Water Treatment, *Appl. Catal. B* **2019**, *248*, 120.

27. Xiao, P.; Zhu, J.; Zhao, D.; Zhao, Z.; Zaera, F.; Zhu, Y., Porous LaFeO₃ Prepared by an in Situ Carbon Templating Method for Catalytic Transfer Hydrogenation Reactions, *ACS Appl. Mater. Inter.* **2019**, *11* (17), 15517.

28. Rao, Y.; Zhang, Y.; Fan, J.; Wei, G.; Wang, D.; Han, F.; Huang, Y.; Croué, J.-P., Enhanced Peroxymonosulfate Activation by Cu-Doped LaFeO₃ with Rich Oxygen Vacancies: Compound-Specific Mechanisms, *Chem. Eng. J.* **2022**, *435*, 134882.

29. Taylor, F. H.; Buckeridge, J.; Catlow, C. R. A., Screening Divalent Metals for A- and B-site Dopants in LaFeO₃, *Chem. Mater.* **2017**, *29* (19), 8147.

30. Nishihata, Y.; Mizuki, J.; Akao, T.; Tanaka, H.; Uenishi, M.; Kimura, M.; Okamoto, T.; Hamada, N., Self-Regeneration of a Pd-Perovskite Catalyst for Automotive Emissions Control, *Nature* **2002**, *418* (6894), 164.

31. Hamada, I.; Uozumi, A.; Morikawa, Y.; Yanase, A.; Katayama-Yoshida, H., A Density Functional Theory Study of Self-Regenerating Catalysts LaFe_(1-x)M_(x)O_(3-y) (M = Pd, Rh, Pt), *J. Am. Chem. Soc.* **2011**, *133* (46), 18506.

32. Shikha, P.; Kang, T. S.; Randhawa, B. S., Effect of Different Synthetic Routes on the Structural, Morphological and Magnetic Properties of Ce Doped LaFeO₃

Nanoparticles, *J. Alloys Compd.* **2015**, 625, 336.

33. Sun, W.; Wei, H.; yang An, L.; Jin, C.; Wu, H.; Xiong, Z.-a.; Pu, C.; Sun, C., Oxygen Vacancy Mediated $\text{La}_{1-x}\text{Ce}_x\text{FeO}_{3-\delta}$ Perovskite Oxides as Efficient Catalysts for CWAO of Acrylic Acid by A-site Ce Doping, *Appl. Catal. B* **2019**, 245, 20.

34. Danielis, M.; Betancourt, L. E.; Orozco, I.; Divins, N. J.; Llorca, J.; Rodríguez, J. A.; Senanayake, S. D.; Colussi, S.; Trovarelli, A., Methane Oxidation Activity and Nanoscale Characterization of Pd/CeO₂ Catalysts Prepared by Dry Milling Pd Acetate and Ceria, *Appl. Catal. B* **2021**, 282, 119567.

35. Lu, J.; Chen, Q.; Chen, S.; Jiang, H.; Liu, Y.; Chen, R., Pd Nanoparticles Loaded on Ceramic Membranes by Atomic Layer Deposition with Enhanced Catalytic Properties, *Ind. Eng. Chem. Res.* **2020**, 59 (44), 19564.

36. Boukha, Z.; Choya, A.; Cortés-Reyes, M.; de Rivas, B.; Alemany, L. J.; González-Velasco, J. R.; Gutiérrez-Ortiz, J. I.; López-Fonseca, R., Influence of the Calcination Temperature on the Activity of Hydroxyapatite-Supported Palladium Catalyst in the Methane Oxidation Reaction, *Appl. Catal. B* **2020**, 277, 119280.

37. Goodman, E. D.; Johnston-Peck, A. C.; Dietze, E. M.; Wrasman, C. J.; Hoffman, A. S.; Abild-Pedersen, F.; Bare, S. R.; Plessow, P. N.; Cargnello, M., Supported Catalyst Deactivation by Decomposition into Single Atoms Is Suppressed by Increasing Metal Loading, *Nat. Catal.* **2019**, 2, 748.

38. Xilan, F.; Dapeng, L.; Baolin, Y.; Mingzhe, S.; Zhimin, H.; Guobao, Y.; Haohan, Y.; Yu, Z., Highly Active PdO/Mn₃O₄/CeO₂ Nanocomposites Supported on One Dimensional Halloysite Nanotubes for Photoassisted Thermal Catalytic Methane Combustion, *Angew. Chem. Int. Ed.* **2021**, 60, 1.

39. Mkhwanazi, T. P. O.; Farahani, M. D.; Mahomed, A. S.; Singh, S.; Friedrich, H. B., Engineering of Catalytic Sites of Pd_x-Ce_{1-x}O_{2-δ} for Dehydrogenation, Oxygen Insertion

and Reverse Water Gas Shift Reactions during Methane Combustion, *Appl. Catal. B.* **2020**, 275, 119118.

40. Zheng, Y.; Xiao, H.; Li, K.; Wang, Y.; Li, Y.; Wei, Y.; Zhu, X.; Li, H. W.; Matsumura, D.; Guo, B.; He, F.; Chen, X.; Wang, H., Ultra-Fine CeO₂ Particles Triggered Strong Interaction with LaFeO₃ Framework for Total and Preferential CO Oxidation, *ACS Appl. Mater. Inter.* **2020**, 12 (37), 42274.

41. Chen, M.; Wang, C.; Wang, Y.; Tang, Z.; Yang, Z.; Zhang, H.; Wang, J., Hydrogen Production from Ethanol Steam Reforming: Effect of Ce Content on Catalytic Performance of Co/Sepiolite Catalyst, *Fuel* **2019**, 247, 344.

42. Tian, N.; Tian, X.; Nie, Y.; Yang, C.; Zhou, Z.; Li, Y., Enhanced 2, 4-Dichlorophenol Degradation at pH 3–11 by Peroxymonosulfate via Controlling the Reactive Oxygen Species over Ce Substituted 3D Mn₂O₃, *Chem. Eng. J.* **2019**, 355, 448.

43. Karvonen, L.; Valkeapää, M.; Liu, R.-S.; Chen, J.-M.; Yamauchi, H.; Karppinen, M., O-K and Co-L XANES Study on Oxygen Intercalation in Perovskite SrCoO_{3-δ}, *Chem. Mater.* **2009**, 22 (1), 70.

44. Lafuerza, S.; Subias, G.; Garcia, J.; Di Matteo, S.; Blasco, J.; Cuartero, V.; Natoli, C. R., Origin of the Pre-peak Features in the Oxygen K-Edge X-Ray Absorption Spectra of LaFeO₃ and LaMnO₃ Studied by Ga Substitution of the Transition Metal Ion, *J. Phys. Condens. Matter* **2011**, 23 (32), 325601.